JGR Oceans

RESEARCH ARTICLE
10.1029/2022JC019051

Temperature Variability and Eddy-Flow Interaction in the South of Oyashio Extension

Haiyuan Yang[1,2], Ruichen Zhu[1,2], Zhaohui Chen[1,2], Jianchao Li[1,3], and Lixin Wu[1,2]

[1]Frontier Science Center for Deep Ocean Multi-spheres and Earth System (FDOMES) and Physical Oceanography Laboratory, Ocean University of China, Qingdao, China, [2]Laoshan Laboratory, Qingdao, China, [3]Laboratory of Fisheries Oceanography, Ocean University of China, Qingdao, China

Abstract Based on observations and eddy-resolving model products, this study investigates the temperature variability south of the Oyashio Extension (OE). During 2016–2021, six dramatic cold events, which significantly impact the local ecosystems, are captured by in situ and satellite observations. It reveals that interaction between the OE front (OEF) and anticyclonic mesoscale eddies originating from the Kuroshio Extension is responsible for these cold events. Accompanied by intense eddy-flow baroclinic energy exchange, the OEF meanders to the south and favors a southward cold-water intrusion. Further analysis illustrates that the cold events tend to occur during spring and autumn, which is associated with the seasonal evolutions of OEF and anticyclonic eddies.

Plain Language Summary To the south of Oyashio Extension (OE), the local temperature plummet and zooplankton increase are recorded by a subsurface mooring. The interaction between Oyashio Extension front and mesoscale eddies drives a southward intrusion of subarctic cold water, leading to local temperature plummet and zooplankton increase. This study highlights the role of mesoscale eddies in regulating the ocean circulation and sheds light on understandings of ocean dynamics on local ecology in Kuroshio-Oyashio Extension region.

Haiyuan Yang and Ruichen Zhu contributed equally to this work.

Key Points:

- Temperature plummet and zooplankton increase are captured by a subsurface mooring to the south of Oyashio Extension
- The development of Oyashio Extension front meander and its interaction with eddies account for the temperature variability
- The eddy-flow interaction is characterized by strong baroclinic energy exchange

Correspondence to:
Z. Chen,
chenzhaohui@ouc.edu.cn

Citation:
Yang, H., Zhu, R., Chen, Z., Li, J., & Wu, L. (2022). Temperature variability and eddy-flow interaction in the south of Oyashio Extension. *Journal of Geophysical Research: Oceans*, *127*, e2022JC019051. https://doi.org/10.1029/2022JC019051

Received 23 JUL 2022
Accepted 3 NOV 2022

1. Introduction

The Oyashio Current, western boundary current of the subarctic North Pacific, carries fresh and cold water southward along the coast of Russia and Japan. In the east of Honshu island, the Oyashio veers eastward with two meanders from nearshore to east, called First Oyashio Intrusion and Second Oyashio Intrusion (Kawai, 1972). After separating from the western boundary, it flows into the open North Pacific Ocean and is renamed as the Oyashio Extension (OE). In comparison to the Kuroshio Extension that is strong in sea surface height (SSH) expressions, the OE is characterized by intense sea surface temperature (SST) and salinity fronts. Observations further prove that the OE involves two quasi-permanent SST fronts (OEF; Isoguchi et al., 2006; Qiu et al., 2017): the western front locates at 145°E−153°E and is thought to be the continuation of Oyashio (Figure 1a; Kawai, 1972; Mitsudera et al., 2018; Miyama et al., 2018; Nishikawa et al., 2021; Wagawa et al., 2020); the eastern one appears between 153°E and 173°E and is important in the midlatitude ocean–atmosphere interaction (Frankignoul et al., 2011; Kwon et al., 2010; Taguchi et al., 2009). Characterized by these complex dynamics and thermohaline structure, the OE is found to be important in regulating the local oceanic environment and climate (e.g., Hasegawa et al., 2019; Ma et al., 2015; Mizuno & White, 1983; Qiu & Chen, 2005; Yang et al., 2019).

As the most prominent component of subpolar gyre, the dynamical state of OEF is strongly linked to the basin-scale wind forcing and local Ekman pumping (e.g., Kwon & Deser, 2007; Nakamura & Kazmin, 2003; Nonaka et al., 2008; Yuan & Talley, 1996). The SSH anomalies induced by wind stress curl in the midlatitude North Pacific basin propagate to western boundary at a speed of the long baroclinic Rossby wave, directly modulating the meridional shift and intensity change of OEF. More recently, Wu et al. (2019) found that the OEF shifted northward in the past four decades because of the poleward expansion and intensification of trade winds. Besides the atmosphere forcing, the OEF is influenced by the Kuroshio Extension as well. Qiu et al. (2017) suggested that the Kuroshio Extension sheds energetic eddies northward and significantly regulates the temperature and circulation fields in the vicinity of OEF, especially the above-mentioned western front. However, their study is mainly based on empirical orthogonal function (EOF) and regression analysis. How the eddies interact with the OEF needs to be further explored.

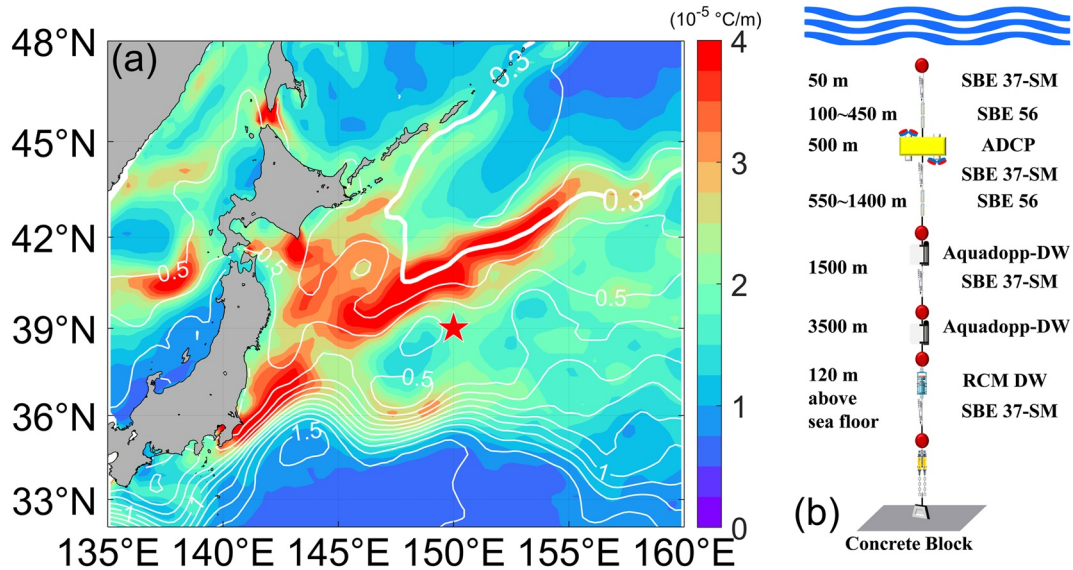

Figure 1. (a) Mean sea surface height (SSH) field (Unit: m; white contours) surrounding the Kuroshio and Oyashio Extension region from 2016 to 2021. The thick white line denotes the contour of 0.3 m and the contour interval is 0.1 m. Color shading indicates the magnitude of the horizontal sea surface temperature (SST) gradient during the same period. The red pentagram denotes the location of M2 mooring. (b) Schematic of the design of M2.

To address the above issues, we have analyzed a five-year subsurface mooring to the south of OEF and found that the large temperature variability is associated with the interaction between OE and mesoscale eddies. The rest of this paper is organized as follows. In Section 2, we will give a brief introduction of the data used in this study. Section 3 describes the observed cold anomalies and OE southward meanders; a detailed analysis of the underlying mechanism is presented. In Section 4, we discuss the biomass response and occurring time of cold events under the joint effect of eddies and OEF. This paper ends with a summary in Section 5.

2. Data

2.1. Mooring Data

In April 2016, a subsurface mooring (named as M2; Figure 1a) was deployed in the south of western OEF (39°N, 150°E) by Ocean University of China. Each year a new set of subsurface mooring with identical configuration replaced the previous one after recovery. M2 is equipped with a suite of CTDs, temperature loggers and current meters for long-term hydrographic data acquisition in the Kuroshio-Oyashio mixed water region (Figure 1b). Here, the data in upper 600 m obtained by two CTDs (SBE 37-SM), five temperature loggers (SBE 56) and two ADCPs (RDI Workhorse Long Ranger 75 kHz) are used. Specifically, the CTDs and temperature loggers with a sampling interval of 5 minutes are set between 50 and 500 m. All temperature records are hourly averaged and then interpolated onto a vertical grid of 25 m. The profiles of echo amplitude are collected hourly by an up-looking ADCP at 500 m in 16-m depth bins. According to Deines (1999) and Mullison (2017), the backscatter coefficient can be estimated from echo amplitude for characterizing the zooplankton population in the water column. To date, five years of data have been successfully retrieved, except for echo amplitude data gap between October 2019 and June 2020 due to incorrect instrument setup. In this study, we focus on motions with frequency higher than one year. For a variable A, the high-frequency component A' is obtained by a high-pass filtering for 300 days.

2.2. Other Observation Products

To access the surface temperature variability in this region, the sea surface temperature (SST) data obtained from the NOAA 1/4° daily Optimum Interpolation Sea Surface Temperature (OISST; Huang et al., 2020) is used. This product has a temporal coverage from 1982 to 2021 and merges observations from different platforms (satellites, ships, buoys and Argo floats) into a regular global grid. The 1/4° daily SSH and absolute surface geostrophic

velocity derived from Archiving, Validation, and Interpretation of Satellite Data in Oceanography (AVISO) are applied to describe the characteristics of mesoscale eddies. The 4-km daily 'cloud-free' Chlorophyll data from GlobColour project is used to study the relationship between the phytoplankton biomass and temperature change. In addition, the World Ocean Atlas 2018 (WOA18; Boyer et al., 2018) temperature and salinity products are also applied to characterize the water mass properties. The following discussion is based on these observations within the domain of (30°N–50°N, 135°E−160°E).

2.3. Model Data

To explore the underlying mechanism of temperature variability in the south of OE region, we examine the multidecadal hindcasts from the Ocean General Circulation Model for the Earth Simulator (OFES; Sasaki et al., 2008). The OFES model is based on Modular Ocean Model version 3 (MOM3) with atmospheric forcing from the National Centers for Environmental Prediction–National Center for Atmospheric Research (NCEP–NCAR) reanalysis (Kistler et al., 1999). It has an eddy-resolving horizontal resolution of 1/10°, covering the global domain from 75°S to 75°N. In the vertical direction, there are 54 levels with thickness varying from 5 m at the surface to 330 m near the bottom. Bottom topography is set based on 1/30° bathymetry data provided from the Ocean Circulation and Advanced Modeling Project (OCCAM). A scale-selective damping with the biharmonic operator is utilized for horizontal mixing of momentum and tracers. The K-profile parameterization vertical mixing scheme from Large et al. (1994) is employed to parameterize subgrid-scale vertical mixing processes. Because of its good performance in simulating the oceanic processes in the Kuroshio-Oyashio Extension, OFES datasets have been widely used for studying the dynamics of ocean circulation and mesoscale eddies in this region (e.g., Nonaka et al., 2006; Qiu et al., 2008; Sato et al., 2016; Taguchi et al., 2010; Xu et al., 2016). In this paper, the 3-day output of upper-250 m oceanic temperature, salinity, velocities, SSH and heat flux within (30°N–50°N, 135°E−160°E) from 1992 to 2017 is used.

3. Results

Figure 2a shows the time-depth plots of in situ temperature obtained by M2 from April 2016 to June 2021. During the five years, six cold events are recorded: April 2016, October 2016, April 2018, November 2019, April 2020 and March 2021. Each event persists for one to three months and results in a rapid cooling in the almost upper 600 m. Temperature-salinity diagram and negative meridional velocity during cold events further suggest that these cold events are associated with the cold/fresh water from the subpolar gyre (Figures 2b and 2c). Influenced by this significant variability, the leading EOF mode of temperature profiles between 250 m and 600 m explains over 92% of the total variance. The corresponding principal component (PC1) is highly correlated to temperature records at 250 m (T_{250}) with correlation r exceeding 0.95 (Figure 2d). Besides mooring observations, the temperature variance is also examined based on satellite observation. We compare T_{250} with SST averaged in a 1° × 1° box centered at M2 (Figure 2e). It is found that T_{250} does not exhibit an annual cycle as SST. A semi-annual peak appears in the power spectrum of both T_{250} and PC1, indicating the temperature variability at 250 m is not simply regulated by the seasonal evolution of surface flux.

To further characterize the cold events, Figure 3 shows the monthly mean SST and SSH contours in the Kuroshio-Oyashio Extension region in 2016. In accordance with previous studies (Isoguchi et al., 2006; Qiu et al., 2017; Wu et al., 2018, 2019), we calculate the averaged SST gradient along each SST isoline within 144°E−152°E and define the isoline with maximum SST gradient as the OEF in this study (red solid lines in Figure 3). The other definitions based on the maximum meridional SST gradient are also examined, which exhibits the same seasonal evolution of OEF (figures not shown). To present a more visible picture of the temporal evolution of OEF, the SST isolines 2.5°C higher than the OEF are also shown (red dashed lines in Figure 3). Obviously, the OEF meanders to the south in April and October and results in southward intrusion of subarctic cold water, which could be inferred from the large temperature decrease and negative meridional velocities recorded by M2 (Figures 2a and 2c). Similar processes are also found in other cold events (see Figures A1–A4 in the Appendix A).

Since cold water intrusion can be identified from the surface, the composite analysis is applied to characterize this feature more visually base on the SST' in a 1° × 1° box centered at M2 from 1992 to 2021 (Figure 4a). Here we define that a non-cold (cold) event occurs when the normalized SST' is larger (less) than −1, which accounts

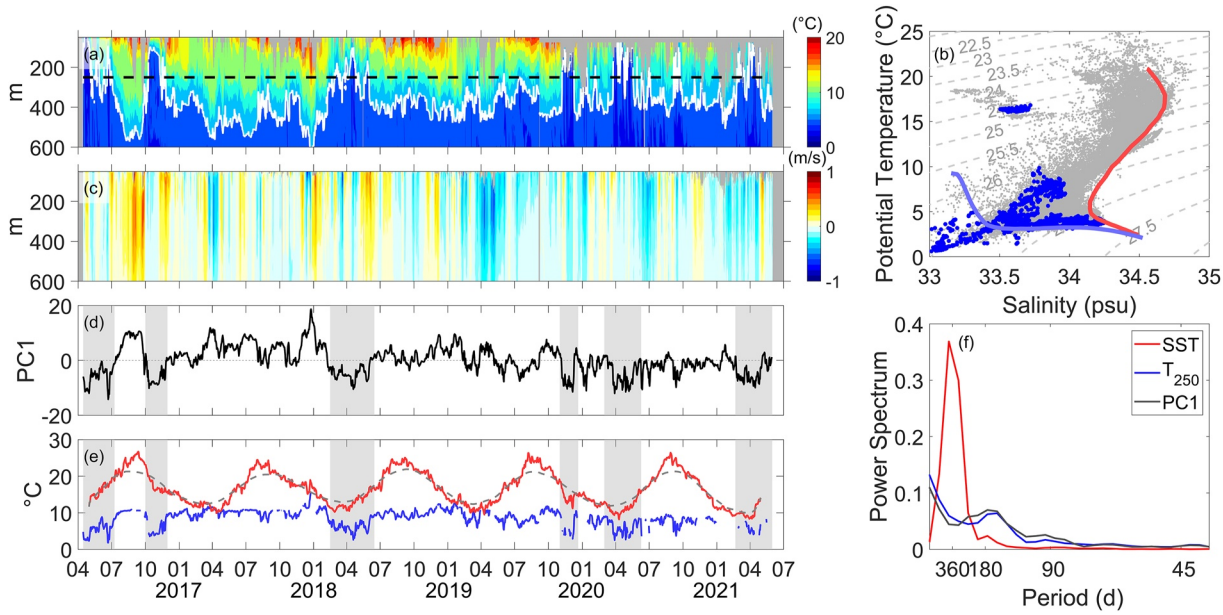

Figure 2. (a) Depth-time plot of temperature after 2-day smoothing from April 2016 to June 2021 by M2. White line is the isotherm of 6°C. The missing records are filled by gray shading. (b) *T-S* diagrams derived from two CTDs at 50m and 400m. The blue dots represent the water mass properties during cold events. The red and blue lines denote the WOA18 climatological water mass properties from Kuroshio (34°N–36°N, 148°E−152°E) and Oyashio (41°N–43°N, 148°E−152°E), respectively. (c) Depth-time plot of meridional velocities for the same period. (d) PC1 of temperature profiles between 250 m and 600 m. (e) Time series of SST (red solid line) and T_{250} (blue solid line). The dashed line indicates the 300-day low-pass filtered SST. The period during temperature plummet is indicated by gray shadings. (f) Power spectrum of SST, T_{250} and PC1.

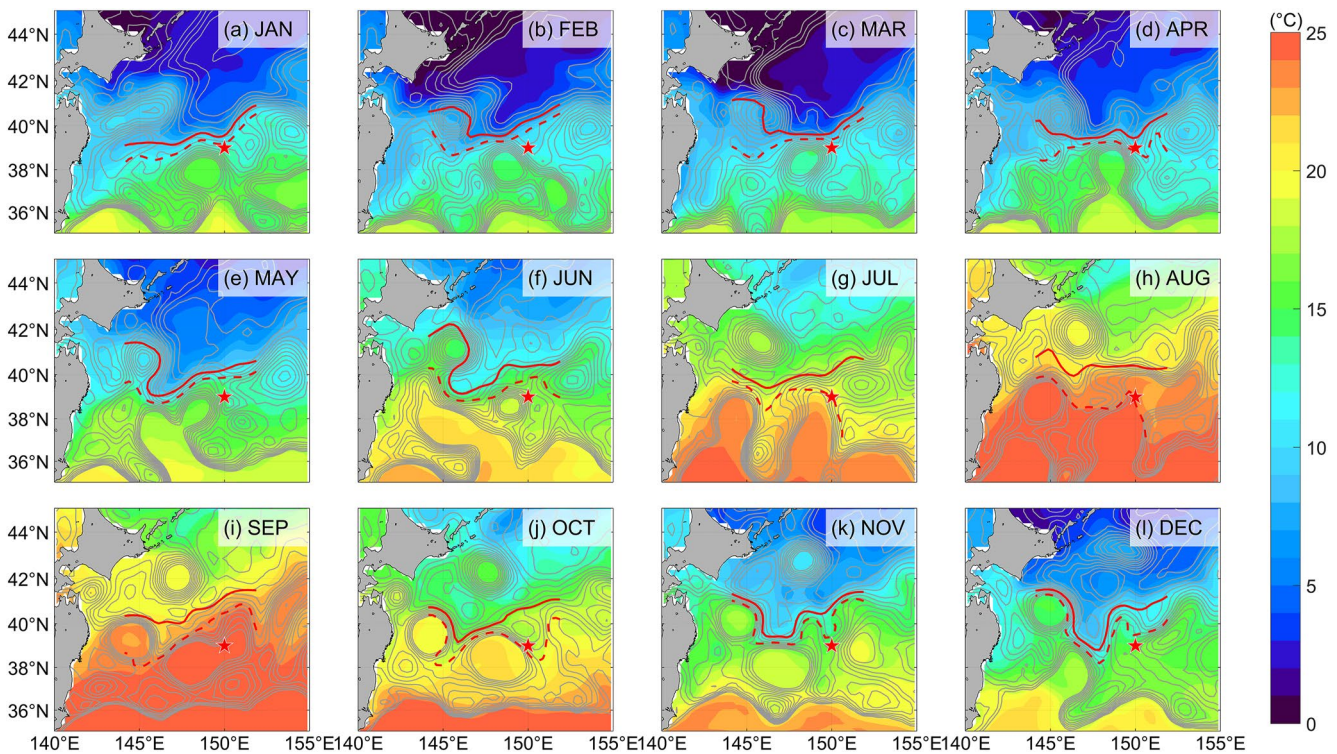

Figure 3. Monthly mean SST fields in 2016. Gray contours denote the monthly mean SSH (Unit: m) and the contour interval is 0.05 m. The red solid line is the SST isoline corresponding to the OEF and the red dashed line is SST contour that is 2.5°C higher than the isoline corresponds to OEF. The red pentagram denotes the location of M2 mooring.

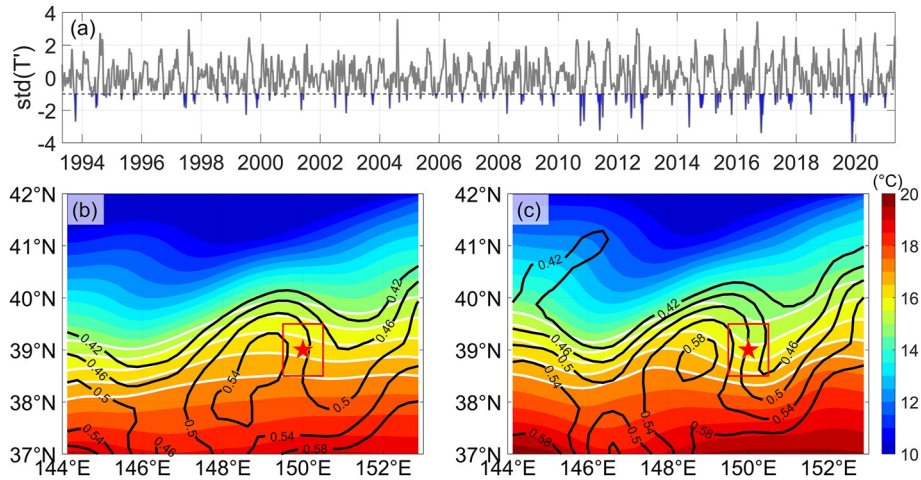

Figure 4. (a) Normalized time series of *SST′* averaged in a 1° × 1° box centered at M2. The area of below one standard deviation is filled in blue, indicating the occurrence of cold events. Mean SST fields in (b) non-cold and (c) cold events. White contours are isolines of 15°C, 15.5°C, 16°C, 16.5°C and 17°C. Black contours denote the mean SSH (Unit: m). The red pentagram denotes the location of M2 mooring and the red rectangle represents the area used to calculate the SST in (a).

for about 85% (15%) of total samples. Figures 4b and 4c compare the composite maps of SST and SSH for the two states, respectively. During non-cold events, SST contours are relatively straight despite SSH contours bending southward around M2. In comparison, SSH contours become denser in cold events, indicating a more developed OE meander and higher current intensity around 150°E (the velocity is 40% stronger in cold events than in non-cold events). SST contours bend to the south as well, which suggests more subarctic water intruding into this region. Accompanied by the evolution of OEF, an anticyclonic circulation adjacent to the west of M2 is also enhanced during cold events (Figures 3d, 3j, and 4). Nishikawa et al. (2021) mentioned that this anticyclonic circulation could interact with OEF and form relatively high eddy kinetic energy (EKE) at approximately 40°N, 150°E, which is considered as a key region of water exchange between the subtropical and subarctic water. During one of cold events, an anticyclonic eddy is found to intensify and approach the OEF in April 2016 (Figures 3a–3d). It provides a favorable condition for the southward bending of OEF path and meanwhile induces a southward intrusion of cold water. After the eddy retreats to the south in May (Figure 3e), the OEF returns to a relatively straight path. The in pace change of OEF path and eddy movement implies that mesoscale eddy is related to the development of meander (similar processes are also found in other cold events). Their interaction will be discussed in the energy budget part.

The temperature variability in the vicinity of OEF is further explored by employing the budget analysis based on OFES model. Before the calculation, we examine the simulation of the front and circulation structure in the OFES output. Both OEF and its southern recirculation can be reasonably reproduced (see Figure B1 in the Appendix B). In addition to the time-mean pattern, the differences between SST and SSH fields during non-cold and cold periods are successfully simulated as well (Figure 5), making OFES a reliable tool for the following research. Following previous studies (e.g., Kwon & Deser, 2007; Pak et al., 2016; Qiu et al., 2017), the governing equation for the upper-ocean temperature is written as

$$\left[\frac{\partial}{\partial t}\left(\frac{1}{H}\int_{-H}^{0} T\,dz\right)\right]' = \left[-\frac{1}{H}\int_{-H}^{0}\left(\underbrace{u\frac{\partial T}{\partial x}}_{ADV_u} + \underbrace{v\frac{\partial T}{\partial y}}_{ADV_v} + \underbrace{w\frac{\partial T}{\partial z}}_{ADV_w}\right)dz\right]' + \left[\frac{Q_{net}}{\rho_0 C_p H}\right]' + \left[\frac{K_h}{H}\int_{-H}^{0}\nabla_h^2 T\,dz - \frac{K_z}{H}\frac{\partial T}{\partial z}\Big|_{z=-H}\right]', \quad (1)$$

where H is the depth of upper ocean and is chosen as 250 m, u, v and w the three-dimensional velocity, Q_{net} the net surface heat flux, ρ_0 the reference seawater density, C_p the specific heat of seawater, K_h (K_z) the horizontal

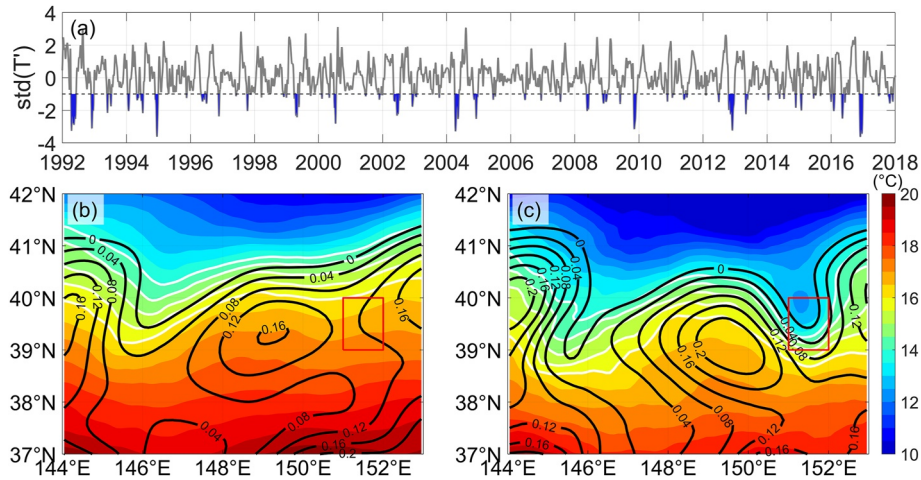

Figure 5. The same as Figure 4 but for OFES output. The red rectangle represents the area (39°N–40°N, 151°E−152°E) used to calculate the SST in (a).

(vertical) eddy diffusivity, and ∇^2 the Laplacian operator. The prime denotes a 300-day high-pass filtering for each term. Physically, the first term on the right-hand side describes the zonal, meridional and vertical advective temperature flux convergence (ADV_u, ADV_v and ADV_w). The second term represents the net heat exchange at the sea surface, and the last two terms are the horizontal and vertical temperature diffusion. As temperature diffusion is not provided in OFES, the last two diffusive temperature terms in Equation 1 are treated as residues in the analysis. It is noted that the locations of the meander and anticyclonic eddy simulated by model are to the northeast of observation (Figure B1). Therefore, we set the center of the 1° × 1° box to 39.5°N, 151.5°E in the temperature budget. Figures 6a and 6b show the budget in these two types of events. The horizontal advection dominants the temperature balance while the air-sea heat exchange and the residue are found to be very small. Compared to non-cold events, the horizontal advection is amplified several times in cold events and the meridional component ADV_v mainly controls the cooling process in this region.

The above analysis has demonstrated that the OEF meander results in the cold events and implied the potential role of mesoscale eddy in its development. To further explore the underlying dynamics of their interaction between meanders and mesoscale eddies, the kinetic energy budget following Chen et al. (2014) is conducted. The governing equation of EKE is

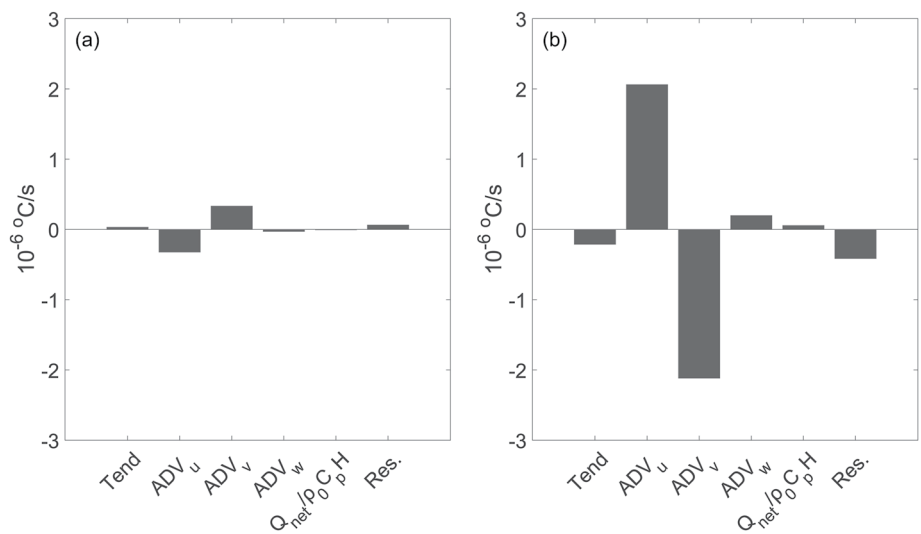

Figure 6. Budget for the temperature during (a) non-cold and (b) cold events after high-pass filtering for 300 days in a 1° × 1° box centered at 39.5°N and 151.5°E in the upper 250 m.

$$\underbrace{\frac{\partial}{\partial t}\left[\frac{\rho_0}{2}\left(u'^2+v'^2\right)\right]}_{\text{Tendency}}+\nabla\cdot\left[\mathbf{u}\frac{\rho_0}{2}\left(u'^2+v'^2\right)\right]+\nabla\cdot\left(\mathbf{u}'p'\right)$$
$$=\underbrace{-g\rho' w'}_{\text{BC}}-\underbrace{\rho_0\left(u'\mathbf{u}'\nabla\bar{u}+v'\mathbf{u}'\nabla\bar{v}\right)}_{\text{BT}}+\rho_0\left(u'D'_u+v'D'_v\right), \quad (2)$$

where the overbar denotes the difference between variable and its 300-day-high-pass value, $\mathbf{u}$ the three-dimensional velocity vector, p the pressure, ρ the sea water density, ρ_0 the reference sea water density, g the gravitational acceleration, D_u and D_v the horizontal momentum diffusion. The terms on the left-hand side represent the temporal change rate of EKE and redistribution rate through advection and pressure work. The terms on the right-hand side are the energy change rate due to baroclinic (BC), barotropic (BT) and friction process, respectively. Here we focus on the contribution of BC and BT terms in energy balance, while the advection and pressure work terms are combined with the diffusion term as residues in the budget. Figure 7 shows the energy budget integrated over upper 250 m in non-cold and cold events. Compared to other terms, the temporal change rate (Figures 7a and 7e) is very small that can be neglected. BC depicts positive values in the domain with high values concentrated along the OEF main axis (Figure 7c). During cold events, two positive spots are found near the eddy edge at 150°E, 40°N and 151°E, 39°N where the OEF changes direction, indicating that the available potential energy is released in these two regions. By contrast, BT is characterized by negative values in the domain, especially in the cold events, suggesting that the eddy helps to maintain the meander. According to Marshall et al. (2012) and Waterman and Jayne (2011), we expect an eddy orientation along the horizontal shear and against the vertical shear. Integrating over the region, magnitude of BC is two times larger than BT, making it dominant in the cold events and eddy-flow interaction.

Besides examining the eddy-mean flow interaction, it is equally important to confirm the source of anticyclonic eddies. Both in observations and OFES outputs (Figures 4c and 5c) during cold events, an anticyclonic signal always appears in the southwest of the OEF meander. We plot in Figure 8a the monthly *T-S* diagrams of the anticyclonic eddies near M2 based on WOA18. It is shown that the water mass properties in the eddy core are more like the Kuroshio water, suggesting that the mesoscale eddies are from the warm/salty subtropical gyre. To determine their origins, the 53 anticyclonic eddies passing by M2 from 1992 to 2021 are tracked based on the closed SSH contours. The shedding position, where the SSH contour is about to close, is recorded manually for each eddy (see Table 1 for details). Figure 8b plots the shedding positions and the black dots represent the eddies relevant to cold events. Most of these positions are distributed in the second crest of Kuroshio (148°E−152°E), where the shedding processes of anticyclonic eddies are frequently observed (Sasaki & Minobe, 2015). The result of eddy tracking here supports the conclusion that western OEF is affected by Kuroshio Extension (Qiu et al., 2017).

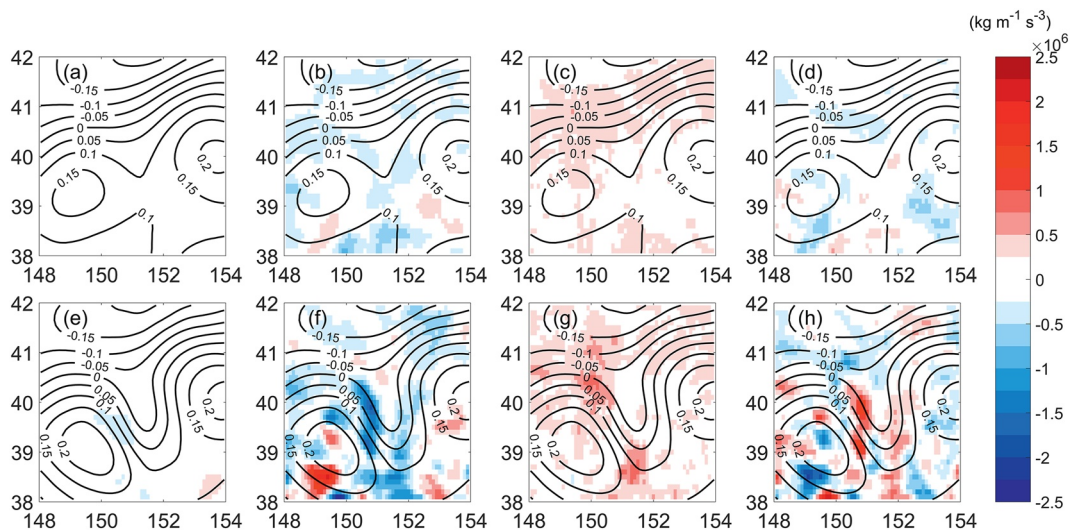

Figure 7. Spatial distribution of (a) temporal change rate, (b) BT term, (c) BC term and (d) residues in non-cold events. (e)–(f) are same as (a)–(d) but in cold events. Black contours denote the mean SSH filed (unit: m).

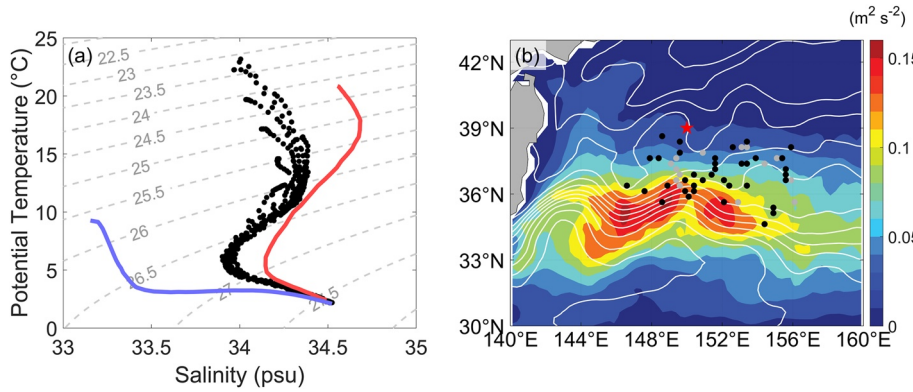

Figure 8. (a) *T-S* diagrams of the anticyclonic eddy (38°N–40°N, 148°E–152°E). The red and blue lines denote the climatological water mass properties from Kuroshio (34°N–36°N, 148°E–152°E) and Oyashio (41°N–43°N, 148°E–152°E), respectively. (b) The shedding positions of anticyclonic eddies passing by M2 from 1992 to 2021. Black (gray) dots denote the eddies passing by M2 when cold (non-cold) events happen. White contours denote the mean SSH and the contour interval is 0.1 m. Color shading indicates the mean EKE. The red pentagram denotes the location of M2 mooring.

4. Discussion

During the observed five-year period, the cold event never happens in late summer (July and August) or late winter (January and February). By detecting the seasonal distribution of cold events during 1992–2021 (Figure 9a), it is found that the cold anomaly tends to appear in late spring (April-June; accounting for 40% of total numbers) and late autumn (October-December; accounting for 39%). The seasonal-locking feature can be well illustrated by plotting the monthly path length of OEF integrated between 146.5°E and 152°E (Figure 9b). It is shown that the OEF meanders twice a year with its length peaking in April and October, which is consistent with the occurring of cold events. It is relevant to ask why the southward meander could develop with cold-water transport in these two seasons? To answer this question, the evolution of OEF is first examined.

Figures 10a and 10b show the annual cycles of OEF intensity and position, which are calculated by averaging SST gradient along the OEF and the mean latitude of OEF, respectively. Compared with the summer counterparts, the OEF intensity and latitudinal position tend to be greater and more southerly in winter, which is induced by the seasonal evolution of atmospheric forcing in the North Pacific Ocean (Hanawa, 1995; Isoguchi & Kawamura, 2006; Sekine, 1988). However, the histograms of OEF intensity and position show only one peak in a single year, failing to explain the double-peak pattern in Figure 9a. Given the strong eddy-mean flow interaction during cold events, the evolution of mesoscale eddy activity could influence the OE variance as well. Figure 10c illustrates that the EKE level is higher in summer than in winter, which is out of phase with temperature variability as well. Therefore, the southward advection of cold water could be attributed to the joint effect of OEF and mesoscale eddies rather than OEF or mesoscale eddies individually.

The dynamical processes are summarized in Figure 11. In winter, the OEF is both strong and shifted to the south, while EKE reaches the lowest level of the year. During this particular period, the OEF can hardly be affected by the mesoscale eddies and keeps a relatively straight path, inhibiting cold water from intruding southward (Figure 11a). In summer, despite the high-level eddy activity, the OEF retreats to the northernmost latitude and the vicinity of M2 is completely taken over by warm water. Thus, there are no more cold events in this region (Figure 11b). During spring and autumn, however, the Kuroshio-Oyashio Extension region undergoes the competition between OEF and eddies. In spring, the westerly becomes weaker and shifts northward with the meridional difference of Q_{net} decreasing (Qiu, 2002). Consequently, the cold subpolar water retreats to the north and the strong OEF becomes weak. To the south of OEF, the anticyclonic eddy begins to develop and generates strong southward flow along its eastern edge. The growing eddy favors the meander of OEF, forming a corridor for cold water flocking southward (Figure 11c). The reverse is true during autumn when the OEF migrates southward and eddy shrinks.

Besides a region abundant with multi-scale oceanic processes, the OE is also an area of high fishing activities. The Hokkaido fishing grounds in the vicinity of OE provide suitable temperature and large amount of nutrients for the ecological environment, supporting a variety of commercially important fishes such as sardine, saury and salmon

Table 1
The Shedding Time and Positions of Anticyclonic Eddies Passing by M2 From 1992 to 2021

Date	Longitude (°E)	Latitude (°N)	Date	Longitude (°E)	Latitude (°N)
1993-09-13	152.4	36.38	2005-12-24	154.4	34.63
1993-10-18	150.4	36.88	2007-07-07	151.4	36.88
1994-05-31	155.6	36.88	2007-11-19	154.9	35.38
1995-07-10	148.6	38.63	2008-10-09	152.1	36.63
1996-08-03	155.9	36.63	2008-11-23	149.9	36.13
1996-10-27	147.6	36.13	2009-07-26	149.4	37.13
1997-01-30	152.1	35.63	2009-10-04	149.4	36.63
1997-09-22	150.4	36.13	2010-04-17	150.4	36.13
1998-07-24	148.9	36.38	2010-09-09	153.4	37.38
1999-06-09	151.6	37.38	2012-04-26	151.6	37.13
1999-08-28	148.4	37.63	2012-12-07	146.6	36.38
1999-10-02	149.6	36.38	2013-02-05	153.4	38.13
2000-03-20	150.1	35.88	2013-08-24	153.4	36.38
2000-07-13	155.6	37.13	2014-06-15	150.4	36.38
2001-02-28	149.4	37.63	2014-06-15	155.6	36.63
2001-06-08	147.9	37.63	2014-11-27	149.6	37.88
2001-08-12	153.1	38.13	2015-09-28	152.6	38.13
2002-05-29	153.9	37.63	2016-07-14	148.6	35.63
2002-10-06	149.6	38.38	2016-10-12	154.4	37.38
2003-06-28	149.6	36.88	2017-02-24	150.9	36.63
2003-12-20	153.1	37.38	2017-10-31	153.4	36.38
2004-02-23	154.9	35.13	2018-02-28	149.9	36.63
2004-03-09	155.1	37.63	2018-05-25	155.4	37.63
2004-04-08	152.9	35.63	2019-05-02	151.6	37.63
2005-02-27	156.1	35.63	2020-08-02	150.9	37.88
2005-06-17	155.9	38.13	2020-10-16	153.4	38.38
2005-07-22	149.1	37.38			

(Sakurai, 2007). Influenced by the front-induced horizontal and vertical mass and heat flux (Chiba et al., 2009, 2013; Yasuda & Watanabe, 1994; Yatsu et al., 2013), the fishery production is in tight connection to the fronts in the OE region (e.g., Mugo et al., 2014; Sassa et al., 2007; Xing et al., 2022). In particular, the meridional migration of OEF in response to the large-scale atmosphere signal (both at seasonal and decadal timescales) significantly influences the local temperature variability and the spatial distribution of fish grounds (Tian et al., 2004, 2014; Yasuda & Watanabe, 1994). In response to the temperature plummet, the surface chlorophyll concentration (*CHL′*) and estimated backscatter coefficient (*BS′*) averaged over upper 200 m have experienced significant increase (Figure 12), suggesting that the temperature variability in M2 could significantly affect the local ecosystem. In addition to cold events, a warm event in December 2017 accompanied by a decrease in *CHL′* and *BS′* is also captured by the mooring. These phenomena suggest that in addition to the seasonal migration of OEF, mesoscale OEF variability can also significantly regulate the local temperature and ecological elements, which could shed light on the prediction of fishery ground.

5. Conclusions

In the present study, observations and eddy-resolving model products are used to investigate the temperature variability in the south of OE. The results show that the OEF meander and its interactions with eddies are important factors regulating the temperature variability and local ecosystems. The main conclusions are summarized as follows:

1. Six cooling processes in the upper ocean are recorded by a subsurface mooring between April 2016 and June 2021. Each cold event can last for one to three months and is accompanied by the negative meridional velocities.
2. Satellite observations and OFES model product show that cold anomalies are associated with the southward meander of OEF, which transports more subarctic water into this region.
3. Accompanied with the development of meander, anticyclonic eddies to its west are also enhanced. Energetics analysis suggests that the eddy-mean flow interaction is enhanced during cold events characterized by strong baroclinic energy exchange. By tracking the source of eddies, it is found that these anticyclonic eddies in this region are mainly originated from the shedding of Kuroshio Extension.

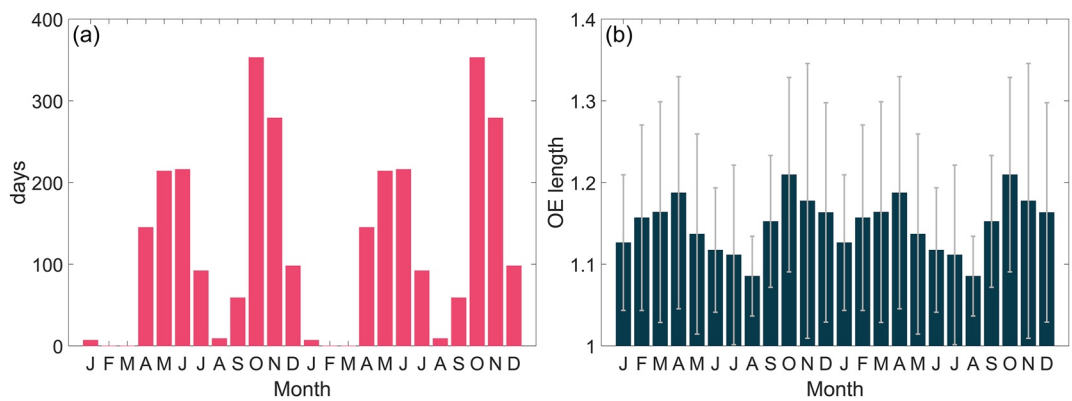

Figure 9. (a) Seasonal distribution of cold events from 1992 to 2021. (b) The month evolution of the OEF length. For clarity, the annual cycle is repeated twice.

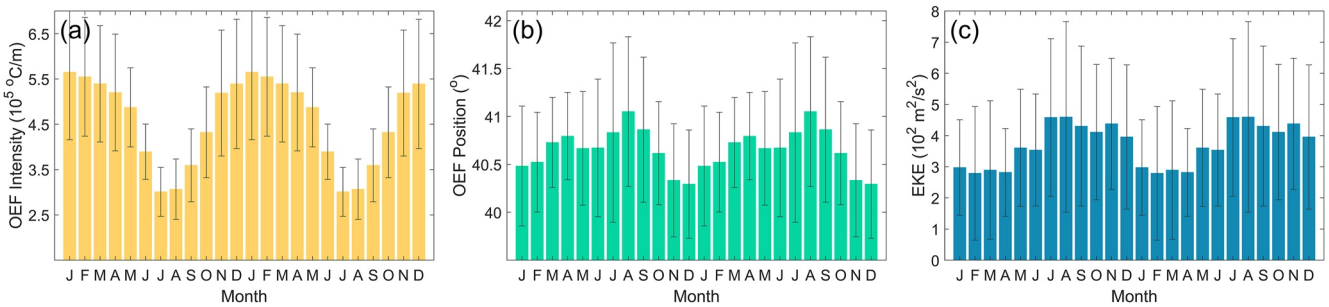

Figure 10. The month evolution of (a) the OEF intensity, (b) the OEF position, and (c) the EKE averaged in a box (37°N–40°N, 147°E−151°E). For clarity, the annual cycle is repeated twice.

4. The cold events tend to appear in spring and autumn and could be explained by the different seasonal evolution between the OEF and mesoscale eddies. The presence of anticyclonic eddies favors the meander of OEF and southward-flowing cold water in spring and autumn. However, this phenomenon disappears in winter when the eddy activity weakens and in summer when the OEF retreats to the north.

This study describes the dynamical processes of temperature variability and implies the potential ecological effect from eddy-flow interaction. A better understanding of these processes will likely be beneficial to predict the evolution of marine ecosystem and fishery. In addition, it should be noted that more observations are required to complete the picture of temperature variability in this region. With the continuous warming, both the Kuroshio Extension and OE are found to migrate northward (Wu et al., 2018; Yang et al., 2020). Whether the phenomenon depicted here exists in the future should be investigated using high-resolution model projections.

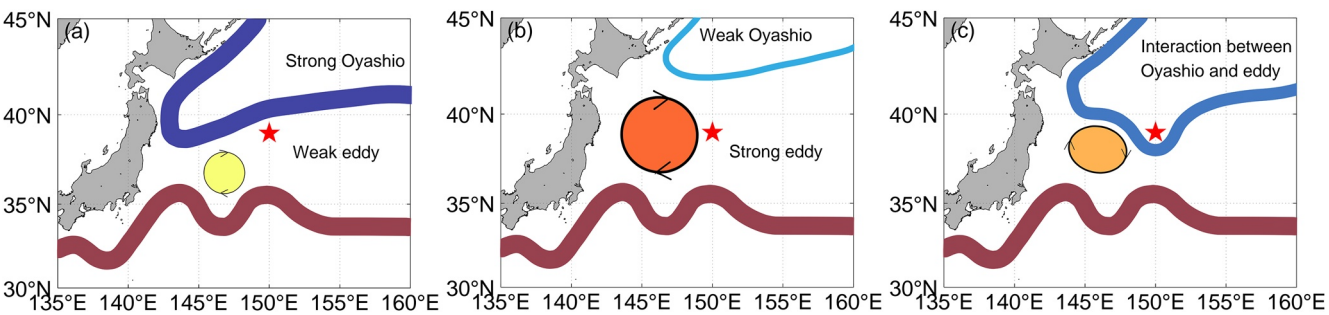

Figure 11. Schematic of the interaction between the OEF and anticyclonic eddies in (a) winter, (b) summer, and (c) spring/autumn.

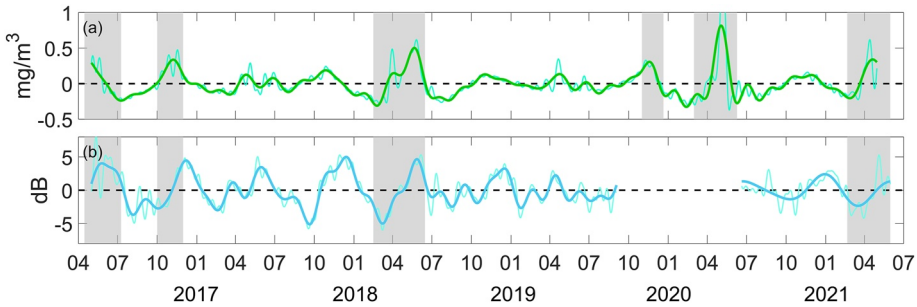

Figure 12. Time series of (a) the surface chlorophyll-a concentration CHL', and (b) the backscatter coefficient BS' averaged over upper 200 m. Primes indicate the high-pass filtering for 300 days. The cases during cold events accompanied by an increase in CHL' and BS' are indicated by gray shadings.

Appendix A: Cold Events Captured by M2 Mooring

In addition to the two cold events in 2016 described in the main text, another four events captured by M2 in April 2018, November 2019, April 2020 and March 2021 are also examined based on the satellite observations. As shown in Figures A1d, A2k, A3d and A4c, the OEF has a common feature of a southward meander, resulting in the cold-water intrusion for one to three months. At the same time, an anticyclonic eddy locates to the west of M2 in favor for the development of meander and southward transport of subarctic water.

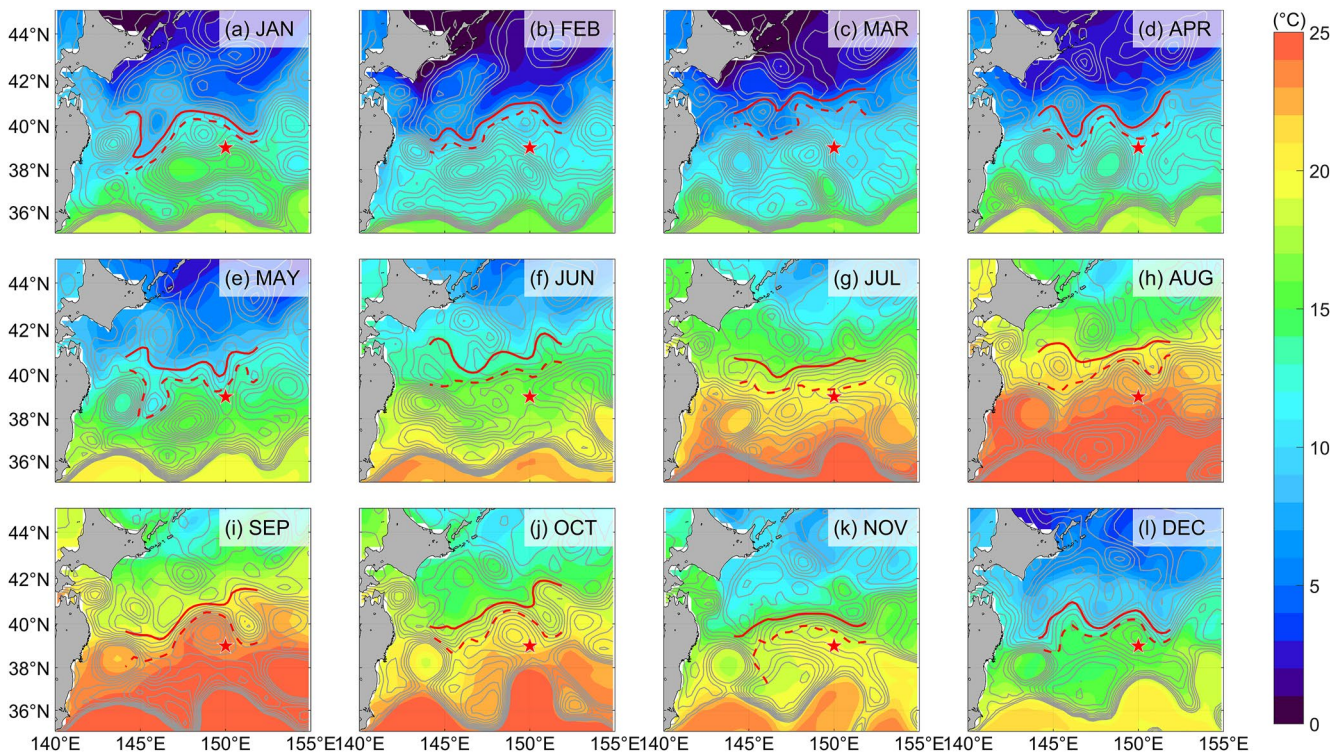

Figure A1. Monthly mean SST fields in 2018. Gray contours denote the monthly mean SSH (Unit: m) and the contour interval is 0.05 m. The red solid line is the SST isoline corresponding to the OEF and the red dashed line is SST contour that is 2.5°C higher than the isoline corresponds to OEF. The red pentagram denotes the location of M2 mooring. Cold event happens in April.

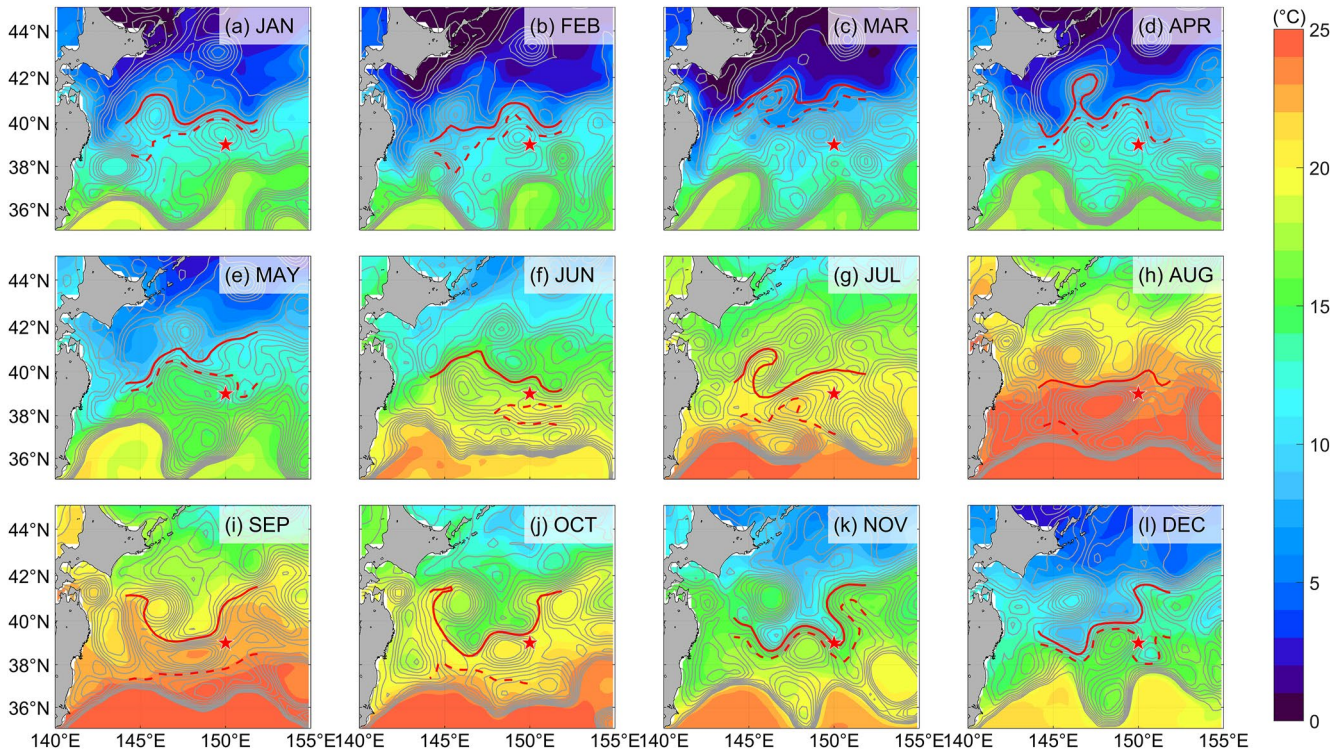

Figure A2. Same as in Figure A1 but for 2019. Cold event happens in November.

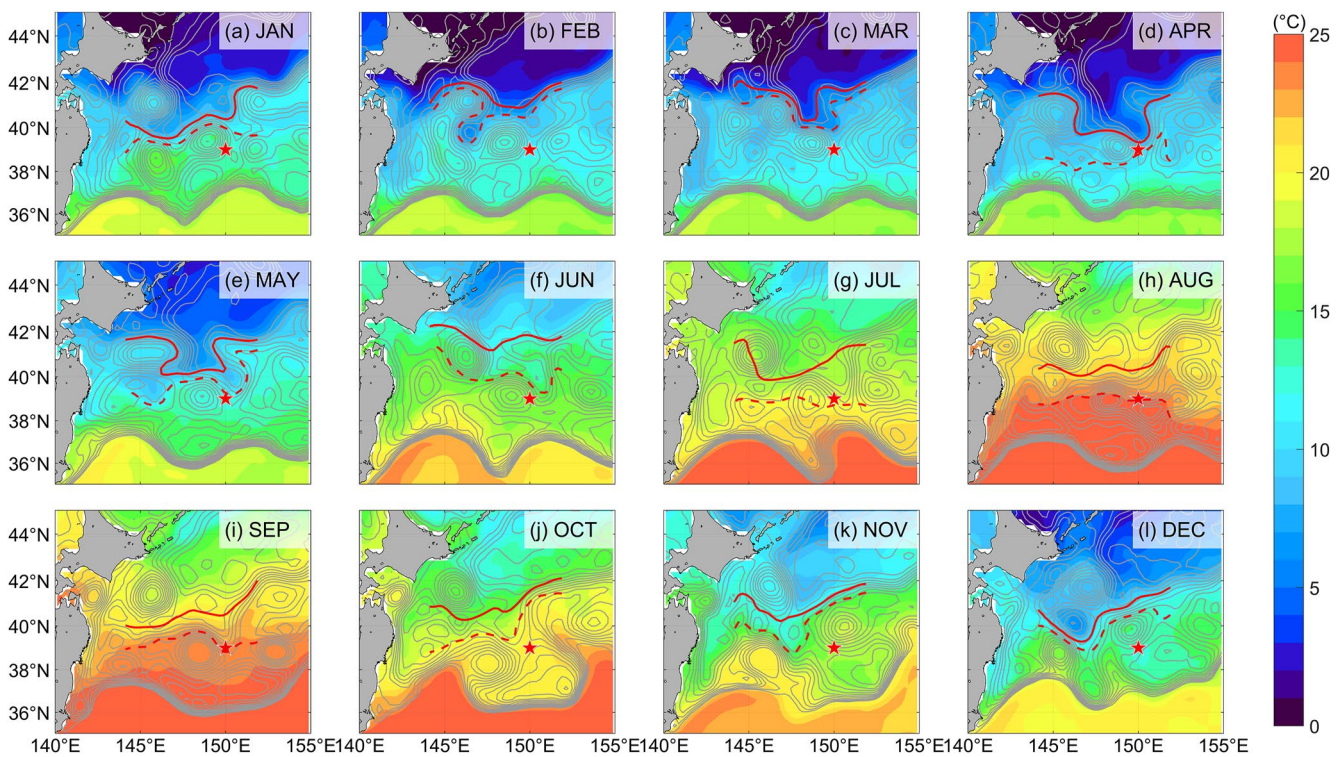

Figure A3. Same as in Figure A1 but for 2020. Cold event happens in April.

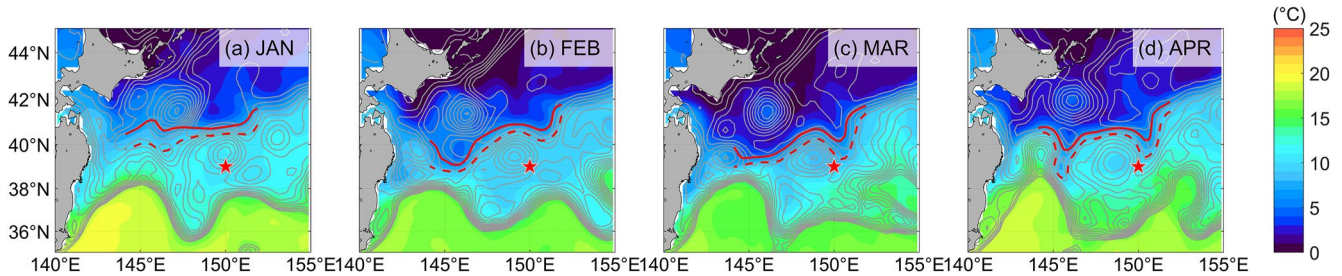

Figure A4. Same as in Figure A1 but for 2021. Cold event happens in March.

Appendix B: Reproducibility of OFES Data

Figure B1 shows that the front and circulation structure can be reasonably simulated in the OFES output. However, the location of the anticyclonic eddy simulated by model is to the northeast of observation. Therefore, we set the center of the 1° × 1° box to 39.5°N and 151.5°E in the OFES data. Based on the same definition of cold events in the observation, the difference in SST and SSH fields between non-cold and cold periods are successfully reproduced. This suggests the choice of (39.5°N, 151.5°E) can be used to explore the dynamic processes associated with cold events in the OFES data.

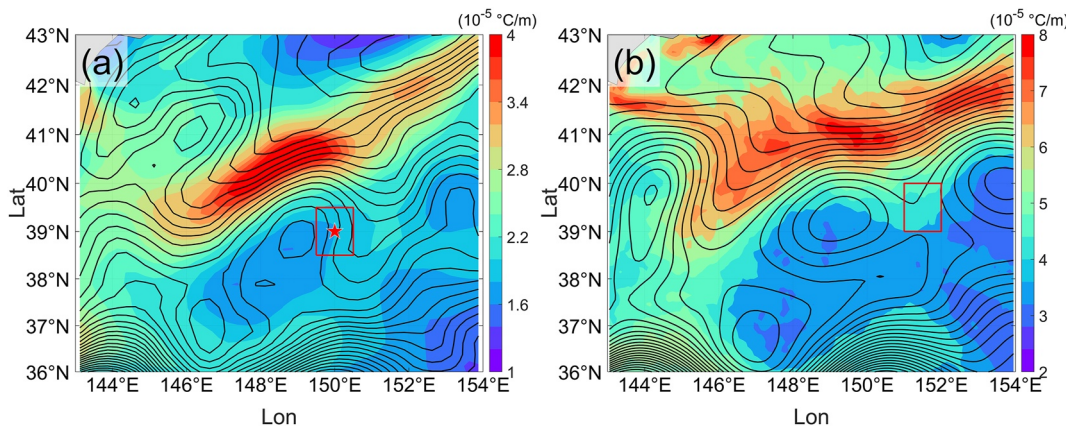

Figure B1. Mean sea surface height (SSH) field (Unit: m; black contours) derived from (a) satellite observation (1992–2021) and (b) OFES output (1992–2017). The contour interval is 0.025 m. Color shading indicates the magnitude of the horizontal sea surface temperature (SST) gradient. The red pentagram denotes the location of M2 mooring and the red rectangle represents the area used to define cold events.

Data Availability Statement

The mooring data can be downloaded via https://www.cn-kems.net/Data/data_figure1.mat. The SST data are available at National Centers for Environmental Information via https://www.ncei.noaa.gov/data/sea-surface-temperature-optimum-interpolation/v2.1/access/avhrr/. Both SSH and Chlorophyll data are obtained from Copernicus Marine Environment Monitoring Service at https://doi.org/10.48670/moi-00148 and https://doi.org/10.48670/moi-00100, respectively, after registering at https://resources.marine.copernicus.eu/registration-form. The WOA18 product is also provided by National Centers for Environmental Information at https://www.ncei.noaa.gov/data/oceans/woa/WOA18/DATA/. The OFES product is downloaded via http://apdrc.soest.hawaii.edu/las_ofes/v6/dataset?catitem=87.

Acknowledgments
This research is funded by National Natural Science Foundation of China (42225601, 42176006, 42076009), Fundamental Research Funds for the Central Universities (842241006; 202072001). Z. C. is partially supported by Taishan Scholar Funds (tsqn201812022).

References

Boyer, T. P., Garcia, H. E., Locarnini, R. A., Zweng, M. M., Mishonov, A. V., Reagan, J. R., et al. (2018). *World Ocean Atlas 2018. Temperature and salinity*. NOAA National Centers for Environmental Information. [Dataset]. Retrieved from https://accession.nodc.noaa.gov/NCEI-WOA18

Chen, R., Flierl, G., & Wunsch, C. (2014). A description of Local and Nonlocal Eddy-Mean Flow Interaction in a Global Eddy-permitting State Estimate. *Journal of Physical Oceanography*, *44*(9), 2336–2352. https://doi.org/10.1175/JPO-D-14-0009.1

Chiba, S., Di Lorenzo, E., Davis, A., Keister, J., Taguchi, B., Sasai, Y., & Sugisaki, H. (2013). Large-scale climate control of zooplankton transport and biogeography in the Kuroshio-Oyashio Extension region. *Geophysical Research Letters*, *40*, 5182–5187. https://doi.org/10.1002/grl.50999

Chiba, S., Sugisaki, H., Nonaka, M., & Saino, T. (2009). Geographical shift of zooplankton communities and decadal dynamics of Kuroshio-Oyashio currents in the western North Pacific. *Global Change Biology*, *15*, 1846–1858. https://doi.org/10.1111/j.1365-2486.2009.01890.x

Deines, K. L. (1999). Backscatter estimation using Broadband acoustic Doppler current profilers. In *Paper presented at the Proceedings of the IEEE Sixth Working Conference on Current Measurement (Cat. No.99CH36331)*. https://doi.org/10.1109/ccm.1999.755249

Frankignoul, C., Sennéchael, N., Kwon, Y.-O., & Alexander, M. A. (2011). Influence of the meridional shifts of the kuroshio and the Oyashio extensions on the atmospheric circulation. *Journal of Climate*, *24*(3), 762–777. https://doi.org/10.1175/2010JCLI3731.1

Hanawa, K. (1995). Southward penetration of the Oyashio water system and the wintertime condition of midlatitude westerlies over the North Pacific. *Bulletin of the Hokkaido National Fisheries Research Institute*, *59*, 103–120.

Hasegawa, T., Nagano, A., Matsumoto, H., Ariyoshi, K., & Wakita, M. (2019). El Niño-related sea surface elevation and ocean bottom pressure enhancement associated with the retreat of the Oyashio southeast of Hokkaido, Japan. *Marine Geophysical Research*, *40*, 505–512. https://doi.org/10.1007/s11001-019-09392-8

Huang, B., Liu, C., Banzon, V., Freeman, J., Graham, G., Hankins, B., & Zhang, H.-M. (2020). Improvements of the Daily Optimum Interpolation Sea Surface Temperature (DOISST) Version 2.1. *Journal of Climate*, *34*, 1–47. https://doi.org/10.1175/JCLI-D-20-0166.1

Isoguchi, O., & Kawamura, H. (2006). Oyashio seasonal intensification and its effect on subsurface temperature variation off the Sanriku coast. *Journal of Geophysical Research*, *111*, C10006. https://doi.org/10.1029/2006JC003628

Isoguchi, O., Kawamura, H., & Oka, E. (2006). Quasi-stationary jets transporting surface warm waters across the transition zone between the subtropical and the subarctic gyres in the North Pacific. *Geophysical Research Letters*, *111*, C10003. https://doi.org/10.1029/2005JC003402

Kawai, H. (1972). Hydrography of the Kuroshio Extension. In H. Stommel & K. Yoshida (Eds.), *Kuroshio—Its Physical Aspects* (pp. 235–354). University of Tokyo Press.

Kistler, R., Kalnay, E., Collins, W., Saha, S., White, G., Woollen, J., et al. (1999). The NCEP/NCAR 50-year reanalysis. *Bulletin of the American Meteorological Society*, *82*, 247–267.

Kwon, Y.-O., Alexander, M. A., Bond, N. A., Frankignoul, C., Nakamura, H., Qiu, B., & Thompson, L. A. (2010). Role of the Gulf Stream and Kuroshio–Oyashio Systems in Large-Scale Atmosphere–Ocean Interaction: A Review. *Journal of Climate*, *23*(12), 3249–3281. https://doi.org/10.1175/2010JCLI3343.1

Kwon, Y.-O., & Deser, C. (2007). North pacific decadal variability in the community climate system model Version 2. *Journal of Climate*, *20*, 2416–2433. https://doi.org/10.1175/JCLI4103.1

Large, W. G., McWilliams, J. C., & Doney, S. C. (1994). Oceanic vertical mixing: A review and a model with a nonlocal boundary layer parameterization. *Reviews of Geophysics*, *32*, 363–403. https://doi.org/10.1029/94rg01872

Ma, X., Chang, P. P., Saravanan, R., Montuoro, R., Hsieh, J.-S., Wu, D., et al. (2015). Distant Influence of Kuroshio Eddies on North Pacific Weather Patterns? *Scientific Reports*, *5*, 17785. https://doi.org/10.1038/srep17785

Marshall, D. P., Maddison, J. R., & Berloff, P. S. (2012). A framework for parameterizing eddy potential vorticity fluxes. *Journal of Physical Oceanography*, *42*(4), 539–557. https://doi.org/10.1175/JPO-D-11-048.1

Mitsudera, H., Miyama, T., Nishigaki, H., Nakanowatari, T., Nishikawa, H., Nakamura, T., et al. (2018). Low ocean-floor rises regulate subpolar sea surface temperature by forming baroclinic jets. *Nature Communications*, *9*(1), 1190. https://doi.org/10.1038/s41467-018-03526-z

Miyama, T., Mitsudera, H., Nishigaki, H., & Furue, R. (2018). Dynamics of a Quasi-Stationary Jet along the Subarctic Front in the North Pacific Ocean (the Western Isoguchi Jet): An Ideal Two-Layer Model. *Journal of Physical Oceanography*, *48*(4), 807–830. https://doi.org/10.1175/JPO-D-17-0086.1

Mizuno, K., & White, W. (1983). Annual and interannual variability in the Kuroshio current System. *Journal of Physical Oceanography*, *13*, 1847–1867. https://doi.org/10.1175/1520-0485(1983)013<1847:aaivit>2.0.co;2

Mugo, R. M., Saitoh, S.-I., Takahashi, F., Nihira, A., & Kuroyama, T. (2014). Evaluating the role of fronts in habitat overlaps between cold and warm water species in the western North Pacific: A proof of concept. *Deep Sea Research Part II: Topical Studies in Oceanography*, *107*, 29–39. https://doi.org/10.1016/j.dsr2.2013.11.005

Mullison, J. (2017). Backscatter estimation using broadband acoustic doppler current profilers-updated. Paper presented at the Hydraulic Measurements & Experimental Methods Conference.

Nakamura, H., & Kazmin, A. S. (2003). Decadal changes in the North Pacific oceanic frontal zones as revealed in ship and satellite observations. *Journal of Geophysical Research*, *108*(C3). https://doi.org/10.1029/1999JC000085

Nishikawa, H., Mitsudera, H., Okunishi, T., Ito, S.-i., Wagawa, T., Hasegawa, D., et al. (2021). Surface water pathways in the subtropical–subarctic frontal zone of the western North Pacific. *Progress in Oceanography*, *199*, 102691. https://doi.org/10.1016/j.pocean.2021.102691

Nonaka, M., Nakamura, H., Tanimoto, Y., Kagimoto, T., & Sasaki, H. (2006). Decadal Variability in the Kuroshio–Oyashio Extension Simulated in an Eddy-Resolving OGCM. *Journal of Climate*, *19*(10), 1970–1989. https://doi.org/10.1175/JCLI3793.1

Nonaka, M., Nakamura, H., Tanimoto, Y., Kagimoto, T., & Sasaki, H. (2008). Interannual-to-Decadal Variability in the Oyashio and Its Influence on Temperature in the Subarctic Frontal Zone: An Eddy-Resolving OGCM Simulation. *Journal of Climate*, *21*, 6283–6303. https://doi.org/10.1175/2008JCLI2294.1

Pak, G., Park, Y.-H., Vivier, F., Bourdalle-Badie, R., Garric, G., & Chang, K.-I. (2016). Upper-ocean thermal variability controlled by ocean dynamics in the Kuroshio-Oyashio Extension region: PAK ET AL.: KOE THERMAL VARIABILITY. *Journal of Geophysical Research: Oceans*, *122*(2), 1154–1176. https://doi.org/10.1002/2016JC012076

Qiu, B. (2002). Large-scale variability in the midlatitude subtropical and subpolar North Pacific Ocean: Observations and causes. *Journal of Physical Oceanography*, *32*, 353–375. https://doi.org/10.1175/1520-0485(2002)032<0353:lsvitm>2.0.co;2

Qiu, B., & Chen, S. (2005). Variability of the Kuroshio extension jet, recirculation gyre, and mesoscale eddies on decadal time scales. *Journal of Physical Oceanography*, *35*(11), 2090–2103. https://doi.org/10.1175/JPO2807.1

Qiu, B., Chen, S., Hacker, P., Hogg, N., Jayne, S., & Sasaki, H. (2008). The Kuroshio extension northern recirculation gyre: Profiling float measurements and forcing mechanism. *Journal of Physical Oceanography*, *38*(8), 1764–1779. https://doi.org/10.1175/2008JPO3921.1

Qiu, B., Chen, S., & Schneider, N. (2017). Dynamical links between the decadal variability of the Oyashio and Kuroshio extensions. *Journal of Climate*, *30*, 9591–9605. https://doi.org/10.1175/JCLI-D-17-0397.1

Sakurai, Y. (2007). An overview of the Oyashio Ecosystem. *Deep Sea Research Part II: Topical Studies in Oceanography*, *54*, 2526–2542. https://doi.org/10.1016/j.dsr2.2007.02.007

Sasaki, H., Nonaka, M., Masumoto, Y., Sasai, Y., Uehara, H., & Sakuma, H. (2008). An Eddy-Resolving Hindcast Simulation of the Quasiglobal Ocean from 1950 to 2003 on the Earth Simulator. In K. Hamilton & W. Ohfuchi (Eds.), *High Resolution Numerical Modelling of the Atmosphere and Ocean* (pp. 157–185). Springer. https://doi.org/10.1007/978-0-387-49791-4_10

Sasaki, Y. N., & Minobe, S. (2015). Climatological mean features and interannual to decadal variability of ring formations in the Kuroshio Extension region. *Journal of Oceanography*, *71*(5), 499–509. https://doi.org/10.1007/s10872-014-0270-4

Sassa, C., Kawaguchi, K., & Taki, K. (2007). Larval mesopelagic fish assemblages in the Kuroshio–Oyashio transition region of the western North Pacific. *Marine Biology*, *150*(6), 1403–1415. https://doi.org/10.1007/s00227-006-0434-x

Sato, N., Nonaka, M., Sasai, Y., Sasaki, H., Tanimoto, Y., & Shirooka, R. (2016). Contribution of sea-surface wind curl to the maintenance of the SST gradient along the upstream Kuroshio Extension in early summer. *Journal of Oceanography*, *72*(5), 697–705. https://doi.org/10.1007/s10872-016-0363-3

Sekine, Y. (1988). Anomalous southward intrusion of the Oyashio east of Japan: 1. Influence of the seasonal and interannual variations in the wind stress over the North Pacific. *Journal of Geophysical Research*, *93*, 2247–2255. https://doi.org/10.1029/JC093iC03p02247

Taguchi, B., Nakamura, H., Nonaka, M., & Xie, S.-P. (2009). Influences of the Kuroshio/Oyashio extensions on Air–Sea Heat Exchanges and Storm-Track Activity as Revealed in Regional Atmospheric Model Simulations for the 2003/04 Cold Season. *Journal of Climate*, *22*(24), 6536–6560. https://doi.org/10.1175/2009JCLI2910.1

Taguchi, B., Qiu, B., Nonaka, M., Sasaki, H., Xie, S.-P., & Schneider, N. (2010). Decadal variability of the Kuroshio Extension: Mesoscale eddies and recirculations. *Ocean Dynamics*, *60*(3), 673–691. https://doi.org/10.1007/s10236-010-0295-1

Tian, Y., Uchikawa, K., Ueda, Y., & Cheng, J. (2014). Comparison of fluctuations in fish communities and trophic structures of ecosystems from three currents around Japan: Synchronies and differences. *ICES Journal of Marine Science*, *71*(1), 19–34. https://doi.org/10.1093/icesjms/fst169

Tian, Y., Ueno, Y., Suda, M., & Akamine, T. (2004). Decadal variability in the abundance of Pacific saury and its response to climatic/oceanic regime shifts in the northwestern subtropical Pacific during the last half century. *Journal of Marine Systems*, *52*(1), 235–257. https://doi.org/10.1016/j.jmarsys.2004.04.004

Wagawa, T., Ito, S.-i., Kakehi, S., Shimizu, Y., Uehara, K., Kuragano, T., & Nakano, T. (2020). Flow structure of a quasi-stationary jet in the western subarctic Pacific (the Western Isoguchi Jet). *Deep Sea Research Part I: Oceanographic Research Papers*, *162*, 103346. https://doi.org/10.1016/j.dsr.2020.103346

Waterman, S., & Jayne, S. (2011). Eddy-mean flow interactions in the along-stream development of a western boundary current jet: An idealized model study. *Journal of Physical Oceanography*, *41*, 682–707. https://doi.org/10.1175/2010JPO4477.1

Wu, B., Lin, X., & Qiu, B. (2018). Meridional shift of the Oyashio extension front in the past 36 years. *Geophysical Research Letters*, *45*, 9042–9048. https://doi.org/10.1029/2018GL078433

Wu, B., Lin, X., & Qiu, B. (2019). On the seasonal variability of the Oyashio extension fronts. *Climate Dynamics*, *53*, 7011–7025. https://doi.org/10.1007/s00382-019-04972-1

Xing, Q., Yu, H., Liu, Y., Li, J., Tian, Y., Bakun, A., et al. (2022). Application of a fish habitat model considering mesoscale oceanographic features in evaluating climatic impact on distribution and abundance of Pacific saury (Cololabis saira). *Progress in Oceanography*, *201*, 102743. https://doi.org/10.1016/j.pocean.2022.102743

Xu, L., Li, P., Xie, S.-P., Liu, Q., Liu, C., & Gao, W. (2016). Observing mesoscale eddy effects on mode-water subduction and transport in the North Pacific. *Nature Communications*, *7*(1), 10505. https://doi.org/10.1038/ncomms10505

Yang, H., Chang, P. P., Qiu, B., Zhang, Q., Wu, L., Chen, Z., & Wang, H. (2019). Mesoscale air–sea interaction and its role in eddy energy dissipation in the Kuroshio extension. *Journal of Climate*, *32*(24), 8659–8676. https://doi.org/10.1175/JCLI-D-19-0155.1

Yang, H., Lohmann, G., Krebs-Kanzow, U., Ionita, M., Shi, X., Sidorenko, D., et al. (2020). Poleward shift of the major ocean gyres detected in a warming climate. *Geophysical Research Letters*, *47*(5). https://doi.org/10.1029/2019GL085868

Yasuda, I., & Watanabe, Y. (1994). On the relationship between the Oyashio front and saury fishing grounds in the north-western Pacific: A forecasting method for fishing ground locations. *Fisheries Oceanography*, *3*, 172–181. https://doi.org/10.1111/j.1365-2419.1994.tb00094.x

Yatsu, A., Chiba, S., Yamanaka, Y., Ito, S.-i., Shimizu, Y., Kaeriyama, M., & Watanabe, Y. (2013). Climate forcing and the Kuroshio/Oyashio ecosystem. *ICES Journal of Marine Science*, *70*(5), 922–933. https://doi.org/10.1093/icesjms/fst084

Yuan, X., & Talley, L. (1996). The subarctic frontal zone in the North Pacific: Characteristics of frontal structure from climatological data and synoptic surveys. *Journal of Geophysical Research*, *101508*, 491–16508. https://doi.org/10.1029/96JC01249